ACS APPLIED NANO MATERIALS

www.acsanm.org Article

Zirconia-Based Magnetoplasmonic Nanocomposites: A New Nanotool for Magnetic-Guided Separations with SERS Identification

Anna Del Tedesco, Valentina Piotto, Gabriele Sponchia, Khohinur Hossain, Lucio Litti, Davide Peddis, Alessandro Scarso, Moreno Meneghetti, Alvise Benedetti, and Pietro Riello*

Cite This: *ACS Appl. Nano Mater.* 2020, 3, 1232−1241 Read Online

ACCESS | Metrics & More | Article Recommendations | Supporting Information

ABSTRACT: In the field of nanomaterials, multifunctional nanosystems play a prominent role in many applications as new magnetically recoverable catalysts, information processing, fuel cells, efficient bio/nanosensors, and nanomedicine. Aiming at the obtainment of new nanomaterials for biotechnological applications such as biosensors or theragnostic systems, we present a multifunctional system able to merge different properties in only one nanotool. The system is prepared by loading the pores of mesoporous zirconia nanoparticles with $CoFe_2O_4$, by a wet impregnation method, further modifying the surface of the material with bis(phosphonic acid) to load gold nanoparticles, produced by laser ablation. The obtained nanocomposite functionalized with a SERS probe represents a specific example of a magnetoplasmonic nanosystem. The results show the efficacy of the strategy of exploiting mesoporous zirconia nanoparticles for obtaining magnetoplasmonic nanotools.

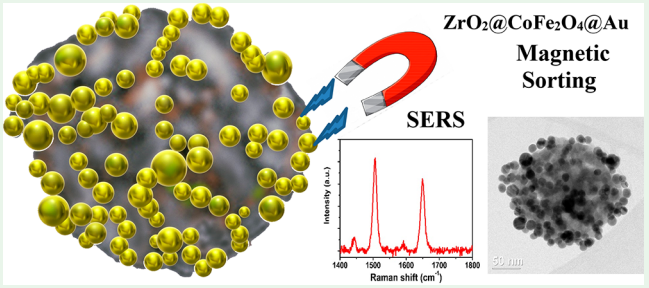

KEYWORDS: *zirconia nanoparticles, $CoFe_2O_4$ nanoparticles, bis(phosphonic acid), gold nanoparticles, magnetic sorting, SERS*

INTRODUCTION

A recent achievement in the field of nanomaterials is represented by the development of multifunctional nanocomposites that, by combining the properties of different materials, allow to one obtain multiple functionalities for specific applications. The combination of different physical−chemical properties in a single nanostructure allows one to greatly expand the fields of application, with just one nanotool. The potential field of application of these multifunctional particles is large, ranging from the realization of multimodal contrast agents for nanomedicine,[1−5] the selective loading, delivery,[5] and detection[6] of therapeutic drugs, and theranostic particles[7−9] to devices for magnetoprocessing of optical information,[10] new and magnetically recoverable catalysts,[11−14] highly efficient nanosensors,[8,15] fuel-cell materials,[16] or Raman dispersion substrates (SERS) with improved surface properties.[2,7,17,18] Furthermore, it is worth underlining that the properties of magnetoplasmonic nanosystems and surfaces can be exploited for their magnetooptical activity.[19,20]

For applications in nanomedicine, a system that could exploit different properties may represent the right answer to the urgent demand for complete theranostic systems and excellent biosensors. Coupling together magnetic and plasmonic properties is an interesting approach to achieving this goal. In this way, a system that acts as a biosensor as well as a theranostic agent can be produced: magnetic properties can be exploited for the separation of analytes from a complex matrix for magnetic resonance imaging measurements or magnetic hyperthermia and the plasmonic ones for the detection of biomolecules, for different imaging techniques, or for plasmonic hyperthermia.[7,21−25] Moreover, SERS signals associated with magnetic nanoparticles are useful for the identification of different analytes, enabling their separation by magnetic sorting.[7,21,26,27] SERS signals show intensities similar to those of fluorescence signals but with some advantages such as narrower peaks with characteristic fingerprints and the absence of bleaching. For this reason, the SERS signal can be easily identified also in complex matrixes typical of in vivo and/or ex vivo experiments.[28,29] High enhancement of the Raman signal, up to 10−14 orders of magnitude,[30] can be achieved with metal nanostructures or nanoparticle arrangements, showing the so-called "hot-spots effect"[31,32] in which the local electromagnetic field can be increased by several orders of magnitude.

On the other hand, when the magnetic properties of such materials are focused on, it is well-known from the literature that Fe ions can interact with a ZrO_2 lattice, stabilizing in this way the tetragonal phase.[33−35] The so-formed solid solution of

Received: October 13, 2019
Accepted: January 15, 2020
Published: January 15, 2020

https://dx.doi.org/10.1021/acsanm.9b01982
ACS Appl. Nano Mater. 2020, 3, 1232−1241

Scheme 1. Schematic Representation of the Work Done from a Chemical Point of View

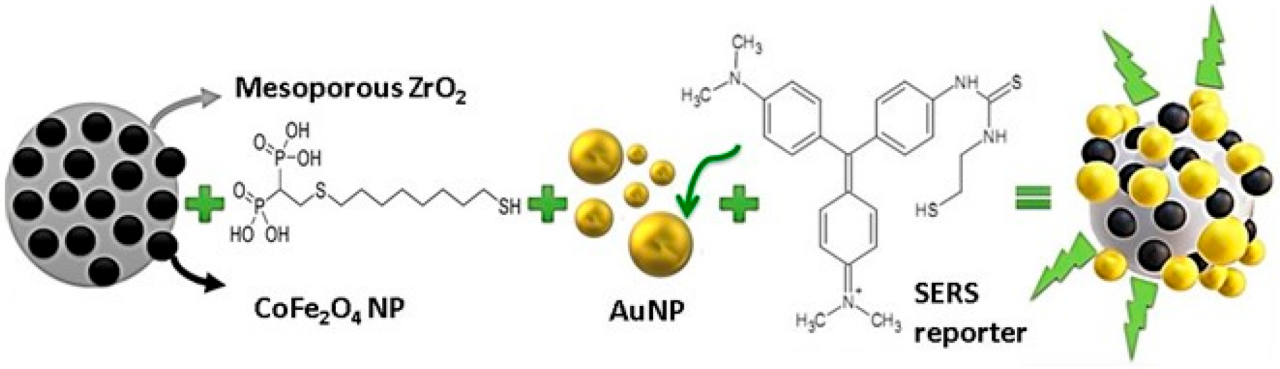

iron and zirconium exhibits peculiar magnetic behavior.[34,36] The high magnetic anisotropy and saturation magnetization of cobalt ferrite [$CoFe_2O_4$] and its behavior at room temperature make this oxide particularly interesting for biomedical applications, despite the presence of cobalt making it potentially toxic if not sufficiently screened.[37−39] However, both functionalization of the surface and inclusion in other more biologically safe matrixes open an interesting prospective for this material in the biomedical field.[40−42]

From the latter considerations, we decided to couple together zirconia and cobalt ferrite following a previously described synthetic route used for the preparation of $CoFe_2O_4$-doped silica,[43] together with gold nanoparticles (AuNPs) obtained by laser ablation.[44]

Furthermore, the resulting magnetoplasmonic nanostructures could be functionalized with organic molecules to target cells or other kinds of structures. As far as cell targeting is concerned, it can be used, for example, for enriching samples of rare cells like circulating tumor cells (CTCs).[7,45]

In the present article, first we describe the preparation methods (see Scheme 1) and the characterization of a system that couples magnetic and plasmonic properties. Subsequently, we define the magnetic behaviors of the nanocomposite, and at the end, we show that SERS can be exploited for controlling the magnetic separation. In the present study, in fact, the magnetic property of the synthesized $CoFe_2O_4$-doped zirconia nanoparticles allows the recovery of a target system, in few minutes, using a common magnet. This property could be very useful in the field of biological sensing; in fact, this approach enables the purification of a very complex matrix, allowing the separation of different analytes. From a biological point of view, it is crucial to avoid interference and to increase the analytical method sensitivity in biological analyses, in particular for biomedical applications, which need to detect analytes at nano- and picomolar concentrations. To increase the sensitivity, we coupled magnetic nanoparticles with SERS-active AuNPs obtained by laser ablation synthesis in solution (LASiS).[44] It is shown that the nanoparticles can be attracted by a laboratory small magnet and that the motion in the presence of a magnetic gradient can be explained with a magnetophoretic model. A proof-of-concept experiment is also reported to show that a mixture of magnetic and nonmagnetic zirconia particles, functionalized with AuNPs, can be efficiently separated and that the sorting can be easily monitored with the SERS signals.

The constructed nanocomposites are new tools that show a new strategic approach based on mesoporous zirconia nanoparticles (MZNs) for obtaining magnetoplasmonic nanosystems that can be profitably exploited in the biotechnology field.

EXPERIMENTAL SECTION

Materials. Zirconium propoxide (Aldrich, 70 wt % in propanol), hexadecylamine (Alfa Aesar, 90%), sodium fluoride (NaF; Eurobio 99%), cobalt nitrate hexahydrate [$Co(NO_3)_2{\cdot}6H_2O$; Janssen Chimica, 99.99%], iron nitrate nonahydrate [$Fe(NO_3)_3{\cdot}9H_2O$; Aldrich, 99.99%], 1,8-octanedithiol (Tokyo Chemical Industry, >97%), bromotrimethylsilane (Sigma-Aldrich, 97%), ethanol (EtOH; Aldrich, 99.8%), and ultrapure water.

Reagents and solvents of high purity were purchased by the providers and used as received. Otherwise, they were purified following the procedures reported in the literature.[46] Anhydrous solvents were prepared by adding activated 3 Å molecular sieves to the specific solvent under an inert atmosphere. Molecular sieves were activated shortly before use by continuous heating under vacuum. Flash chromatography was performed with silica gel Merck 60, 230−400 mesh, following procedures reported in the literature.[47]

Synthesis of MZNs. The synthesis of MZNs has been reported elsewhere.[48] Briefly, a first solution was prepared by dissolving the surfactant in EtOH and adding a second aqueous solution with the correct concentration of dissolved NaF. A third solution of the EtOH precursor was finally added dropwise under vigorous stirring. The precipitate was recovered by centrifugation and washed thoroughly. Finally, the recovered powder was treated under vacuum at 120 °C to remove the residual surfactant, avoiding any modification of the structure of the nanoparticles.

Zirconia Nanoparticles/Iron−Cobalt Oxide [MZN@$CoFe_2O_4$, a Magnetic Mesoporous Zirconia Nanoparticle (mMZN)]. The synthesis of metal oxide doped nanoparticles was adapted from the procedure developed by Parma et al.[43] MZNs (10 mg mL^{-1}) were dispersed in ultrapure water and impregnated using nitrate salt of the desired metal (cobalt or iron) in the proper amount. After stirring overnight, the impregnated materials were dried under vacuum and then annealed at 700 °C for 12 h in air. The synthesized samples are described in Table 1.

Synthesis of AuNPs. AuNPs were synthesized using the LASiS method.[44] LASiS was obtained by focusing (10 cm focal length) 9 ns at 1064 nm of a Nd:YAG (Quantel YG981E, 10 Hz) laser on a pure gold target under a bidistilled water solution of 10^{-5} M NaCl. AuNPs

Table 1. Nominal Compositions of the mMZNs Loaded with Magnetic $CoFe_2O_4$

($CoFe_2O_4$ moles/ZrO_2 moles) × 100	sample name	$CoFe_2O_4$, mol %
4	mMZN-4	3.8
8	mMZN-8	7.4
12.5	mMZN-12.5	11.1

https://dx.doi.org/10.1021/acsanm.9b01982
ACS Appl. Nano Mater. 2020, 3, 1232−1241

were obtained with an average size of 25 nm and a ζ potential of −30 mV. Nanoparticles were easily functionalized thanks to their naked surface.

Synthesis of [2-[(8-Mercaptooctyl)thio]ethane-1,1-diyl]bis-(phosphonic acid) (BPODE). The bis(phosphonic acid) bearing a terminal thiol moiety useful for nanoparticle surface functionalization was prepared following a modified procedure reported in the literature.[49] Details can be found in the Supporting Information.

The synthesis of the bis(phosphonic acid) was followed with a TLC Polygram Sil G/UV254 (0.25 mm thickness). ^{1}H, ^{13}C, and ^{31}P NMR and 2D spectra were recorded with Bruker Avance 300 and Ascend 400 spectrometers, respectively, working at 300−400 MHz for ^{1}H NMR, 75−100 MHz for ^{13}C NMR, and 121−161 MHz for ^{31}P NMR. Resonance frequencies are referred to tetramethylsilane and 85% H_3PO_4.

Functionalization of the Nanoparticles. MZN or mMZN (10 mg mL^{-1}) dispersed in 5 mL of ultrapure water was treated with the desired amount of BPODE (structure reported in the Supporting Information) with a final concentration of 10 mM. The suspension was stirred for 5 h, after which the nanoparticles were filtered and washed with ultrapure water.

Synthesis of the mMZN@AuNPs. A total of 0.7 mg of mMZN-8 nanoparticles, functionalized with BPODE, was dispersed in 1 mL of distilled water. The solution was centrifuged at 800 rcf for 3 min to eliminate aggregates. After magnetic separation, the zirconia-based nanoparticles were dispersed in 1 mL of a AuNPs aqueous colloidal solution (3×10^{-9} M) and synthesized by LASiS (see above). Functionalization of the mMZN-8 nanoparticles with the AuNPs (mMZN@AuNPs) was achieved after sonication for 2 h with the addition of a NaCl solution to a final concentration of 20 mM. Isolation from free AuNPs was achieved by magnetic sorting. Finally, the SERS reporter, malachite green functionalized with a thiol-containing side chain[32] (20 μL at 30 μM), was added to the mMZN@AuNPs dispersed in 1 mL of distilled water. After sonication for 45 min, the mMZN@AuNPs were cleaned three times by magnetic sorting.

Synthesis of the MZN@AuNPs. A total of 0.7 mg of MZNs functionalized with BPODE was centrifuged at 650 rcf for 8 min to eliminate aggregates. Then the supernatant was centrifuged at 25000 rcf for 10 min, and after elimination of the supernatant, 1 mL of a AuNPs aqueous colloidal solution (3×10^{-9} M), synthesized by LASiS, was added. Sonication and a solution of NaCl were used in the case of mMZN@AuNPs. Cleaning from free AuNPs was obtained by centrifugation at 810 rcf for 6 min because denser AuNPs precipitated, whereas MZN@AuNP nanostructures were recovered from the supernatant. Texas Red functionalized with two thiol units[3,32] (20 μL at 30 μM) was added, as a SERS reporter, to 1 mL of MZN@AuNPs in water. After sonication for 45 min, the nanostructures were cleaned three times from the reporter by centrifugation.

Characterization Methods. The obtained nanocomposites were studied by field-emission scanning electron microscopy (FE-SEM), transmission electron microscopy (TEM), powder X-ray diffraction (PXRD), and small-angle X-ray scattering (SAXS).

The size and shape of the nanoparticles were investigated by electron microscopy using a Zeiss Sigma VP field-emission scanning electron microscope, equipped with a Bruker Quantax energy-dispersive X-ray (EDX) spectrometry microanalysis detector. *ImageJ* software was used to evaluate the size of the nanoparticles: a minimum of 100 particles were used to determine the size distribution of all analyzed samples.[50,51]

TEM images were taken with a JEOL 3010 microscope, operating at 300 kV, equipped with a GATAN (Warrendale, PA) multiscan CCD camera. Some drops of the samples ultrasonically dispersed in EtOH (ca. 1 mg mL^{-1}) were deposited on a holey carbon film grid for TEM observation.

The PXRD measurements were performed using nickel-filtered Cu Kα radiation in Bragg−Brentano geometry with a X'Pert goniometer (Philips) equipped with a graphite monochromator. Line-broadening analysis was used to evaluate the crystallite sizes.[52]

SAXS data were collected with a Kratky camera (PAAR) using nickel-filtered Cu Kα radiation. The data were corrected for the absorption effect, and the sample holder scattering was subtracted.

A Micromeritics ASAP 2010 analyzer was used to collect the nitrogen adsorption−desorption isotherms at liquid-nitrogen temperature. The data were analyzed using the Brunauer−Emmett−Teller equation[53] to obtain the specific surface area and the Barrett−Joyner−Halenda model[54] to recover the pore-size distribution.

DRIFT-IR spectra were recorded with a Nexus FT-IR using a Nicolet AVATAR diffuse-reflectance accessory.

An Agilent Cary 5000 spectrophotometer and a quartz cuvette (2 mm optical path) were used to collect the UV−vis−near-IR spectra. SERS spectra in solution were recorded in a 2 mm quartz cuvette with a Renishaw inVia micro-Raman instrument using a 5× objective and a helium−neon laser with a power of 1.5 mW on the cuvette.

ζ-potential measurements were recorded with a Malvern Nano ZS instrument equipped with a 633 nm helium−neon laser.

Direct-current (dc) magnetization measurements were performed with a Quantum Design SQUID magnetometer, equipped with a superconducting coil, which produces magnetic fields in the range of ±5 T. The nanoparticles were dispersed in an epoxy resin to avoid any movement during the measurements.

Magnetophoretic characterization was performed by recording the decreasing UV−vis extinction of a solution of magnetic nanosystems under a magnetic gradient obtained with a small magnet.[21] The solution was inserted into the UV−vis spectrometer in a 3 × 10 × 10 mm^3 (optical path 10 mm) cuvette, whereas the magnet (Supermagnete S-10-20-N; D = 10 mm diameter and h = 20 mm height) was inserted perpendicularly to the optical path and in contact with the solution.

RESULTS AND DISCUSSION

MZNs were successfully obtained by sol gel using a neutral surfactant combined with inorganic salts.[48]

It is worth noticing that, in order to obtain zirconia nanoparticles with large surface area preserving the porosity, the surfactant was removed at 120 °C in a vacuum extraction process. The nanoparticles obtained with this method were amorphous, spherical, and monodispersed, with a mean diameter of 200 nm (Figures 1, left, and S14).

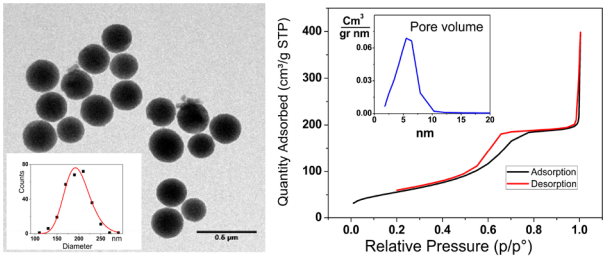

Figure 1. Left: TEM images of MZNs and particle size distribution (inset). Right: Nitrogen physisorption analysis and pore-size distribution before thermal treatment (inset).

The nanoparticles have a surface area of about 200 m^2 g^{-1} with a pore volume of 0.3 cm^3 g^{-1} and a pore diameter distribution centered at 5 nm, sufficiently large to host several types of molecular guests. The isotherms display the type IV profile with a H1 hysteresis loop (according to the IUPAC classification; Figure 1, right),[55] typical for mesoporous materials. If treated at temperatures higher than 300 °C, ZrO_2 crystallizes, with collapse of the structure of the MZNs with a loss of porosity and the formation of large aggregates.[48,56,57]

https://dx.doi.org/10.1021/acsanm.9b01982
ACS Appl. Nano Mater. 2020, 3, 1232−1241

Upon high-temperature treatment (700 °C), the nanoparticles impregnated with cobalt and iron salts do not aggregate and the roundness of the nanoparticles is maintained (Figure 2).

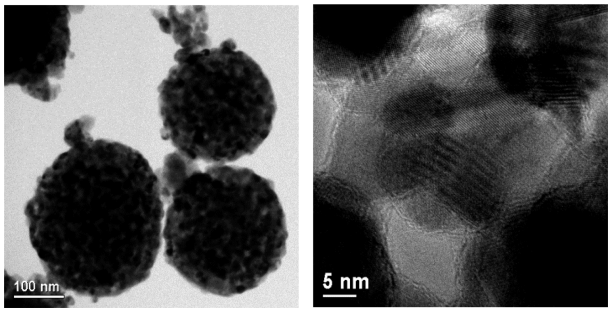

Figure 2. TEM images of mMZN-8.

All samples, after thermal treatment, have a surface area of around 20 m^2 g^{-1} (nitrogen physisorption analysis; Figure S15), 10 times lower than the initial surface area and close to the surface area of full density ZrO_2 nanoparticles of similar size: pores are now filled with metal oxides and/or shrunken because of the crystallization of zirconium oxide.

The sample mMZN-12.5, i.e., with a higher loading of $CoFe_2O_4$, shows a big change in the morphology and microstructure and a large amount of iron and cobalt oxide particles outside the ZrO_2 nanospheres, while the sample mMZN-8 is the best compromise for the microstructure, loading, and presence of cobalt−iron oxide nanoparticles outside the ZrO_2 nanospheres (see the SEM images in Figures S16 and S17).

TEM images of mMZN-8 confirm that the shapes and sizes of the nanoparticles are maintained and show that they have a crystalline microstructure (Figure 2, right) with sizes in the range of 15−30 nm (further confirmed by SAXS and wide-angle X-ray scattering measurements; Table S1).

The PXRD plots in Figure 3 show both the MZN patterns before (amorphous) and after the thermal treatment of mMZN.

Crystallization of MZN (Figure 3d) provides mainly the thermodynamically stable monoclinic ZrO_2 with a very low content of tetragonal ZrO_2 probably stabilized by the small size of the crystallites (Table S1). On the other hand, crystallization of all of the mMZN-X samples produces both tetragonal and monoclinic ZrO_2. Stabilization of the most symmetric tetragonal phase is probably due to the formation of a solid solution between the zirconia and iron or cobalt oxides.[35,58−60] The weight fraction of the tetragonal phase of ZrO_2 increases with the amount of Co and Fe ions until about 70% for the 8% and 12.5% samples (Table 2).

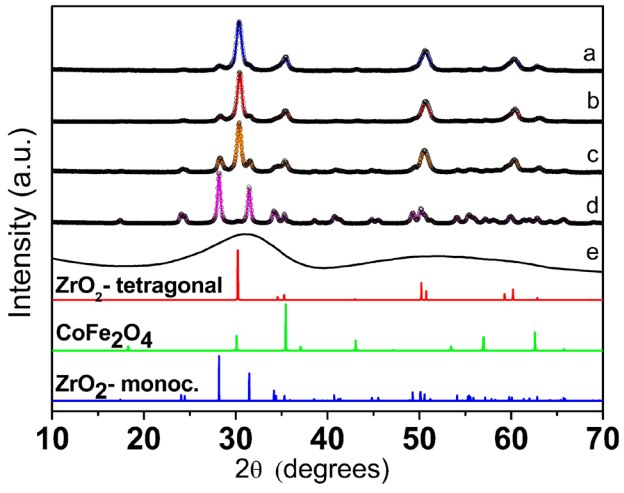

Figure 3. PXRD patterns of (a) mMZN-12.5, (b) mMZN-8, (c) mMZN-4, (d) MZN@700 °C, and (e) amorphous MZN.

Table 2. PXRD Quantities of Different Phases of the Different Samples (in Parenthesis, the Expected Nominal Values)

sample	t-ZrO_2 (wt %)	m-ZrO_2 (wt %)	$CoFe_2O_4$ (wt %)	$CoFe_2O_4$ (mol %)
MZN@700 °C	2	98		
mMZN-4	56	38	6	3.2 (3.8)
mMZN-8	73	19	8	4.4 (7.4)
mMZN-12.5	68	17	15	8.5 (11.1)

Furthermore, the crystalline $CoFe_2O_4$ fraction, determined by Rietveld analysis with some difficulty because of superposition of the peaks (Figure S18), is always lower than the loaded one, in accordance with the hypothesis that part of the iron−cobalt oxides form solid solutions, with ZrO_2 stabilizing the tetragonal zirconia fraction. We can also observe that the missing fraction of cobalt−iron oxide saturated at about 3.0 mol %.

SAXS analysis allows measurement of the sizes of the $CoFe_2O_4$ particles that have an electron density lower than the electronic density of the ZrO_2 matrix.

The size of the large sphere (~200 nm) is higher than the resolution of our Kratky camera, so only the asymptotic h^{-3} behavior (Porod asymptotic law for a slit-smeared camera) is visible as the background.

SAXS data are fitted assuming a distribution of spherical $CoFe_2O_4$ inclusion, and the obtained average sizes agree with the PXRD pattern analyses reported in Table S1: the $CoFe_2O_4$ crystallite sizes are smaller or equal to the sizes of the particles. Figure S19 shows the fit and size distribution obtained for the 8% sample.

DC magnetization measurements with a SQUID magnetometer were also performed (Figure S20). As expected, at low temperature, all of the samples show hysteretic behavior. mMZN-4 shows an evident kink around zero field, together with strong but not saturated character at high field.

This feature can be ascribed to the presence of a soft magnetic phase, probably due to separation of Co_3O_4, as was already observed in the literature,[61] inducing an off-stoichiometry in the $CoFe_2O_4$ nanoparticles. The presence of soft-magnetic-phase mMZN-4 affects the value of the coercivity field (H_c) and, especially, the value of saturation magnetization (M_s) at 300 K, which is extremely low (Table 3) with respect to the other samples, thus confirming the presence of some impurities (e.g., Co_3O_4). Because of the behavior of this sample, it seems to be not physically possible to determine a value of the reduced remanence magnetization (M_r/M_s). On the other hand, samples with 8% and 12.5% of cobalt ferrite show quite high coercivity, compatible with the presence of stoichiometric nanostructured $CoFe_2O_4$.

https://dx.doi.org/10.1021/acsanm.9b01982
ACS Appl. Nano Mater. 2020, 3, 1232−1241

Table 3. DC Magnetization Measurements with a SQUID Magnetometer: Coercive Field ($\mu_0 H_c$), Magnetization Recorded at 5 T (M_{5T}, 5 K), Reduced Remanent Magnetization (M_r/M_s), and Saturation Magnetization Recorded at 300 K (M_s, 300 K)[a]

sample	$\mu_0 H_c$ at 5 K (T)	M_{5T} at 5 K (A m^2 kg^{-1})	M_r/M_s	M_s at 300 K (A m^2 kg^{-1})
mMZN-4	0.92(1)			29(1)
mMZN-8	1.4(2)	88(4)	0.8	63(4)
mMZN-12.5	1.4(2)	68(5)	0.7	51(2)
mMZN-8-BPODE	1.4(2)	91(4)	0.5	45(3)

[a]Uncertainties in the last digit are given in parentheses.

At low temperature, a strong nonsaturating tendency is observed probably because of the high surface anisotropy.[62] However, the values of magnetization measured at 5 T are also compatible with the presence of $CoFe_2O_4$ nanoparticles, with a M_{5T} value for mMZN-8 that is very close to the bulk value (93 A m^2 kg^{-1}),[63] indicating the good quality of the particles in this sample (Table 3). The lowering of M_{5T} with respect of the bulk value observed in mMZN-12.5 can be ascribed to the complex interplay between the surface spin disorder (i.e., spin canting) and cationic distribution.[64] The good magnetic properties of the mMZN-8 sample are confirmed by the value of the reduced remanent magnetization at 5 K around 0.7, which is close to the theoretical value for the cubic anisotropy (M_r/M_s = 0.8) and definitively in agreement with that of the crystalline particles of $CoFe_2O_4$.[65,66] All of the samples show nonzero coercivity and remanence magnetization at 300 K (Figure S20), clearly indicating that at this temperature nanoparticles in the "blocked state" are still present. The value of saturation magnetization confirms again the better performance of the mMZN-8 sample, showing the highest saturation magnetization.

The 8% sample has been successfully functionalized with BPODE, as proven by EDX, IR, ζ-potential, and SQUID analysis. This simple alternative method for functionalization of the metal oxide nanoparticles does not use the organosilane precursors,[67,68] which often also require a silica interface layer to obtain an effective functionalization. DRIFT-IR spectra (Figure 4, left) show changes of the MZNs after functionalization: as one can see in the red line, peaks under 3000 cm^{-1} and around 1000 cm^{-1} were found, corresponding to aliphatic C−H and bounded P−O vibrations, respectively. Moreover, as one can see from the spectra of the bis(phosphonic acid) before coupling (blue line) and of the coupled system (red line), peaks concerning P−O vibrations are shifted at higher wavenumbers, proving the bonding of the molecules on the nanoparticles.[69,70] ζ-potential titrations were also performed to confirm surface modification of the nanoparticles (Figure 4, right). As one can see, charge values change substantially with the samples: MZNs show positive ζ-potential values at acidic pH and negative ones in basic conditions, having an isoelectric point around pH 7.

On the other hand, for modified MZNs, different behavior are shown: they present more negative values of the surface charge at almost all tested pH values. The mMZN-8 samples have slightly positive ζ-potential values at the lowest pH tested, showing an isoelectric point around pH 4.5, and decrease with increasing pH.

This behavior could be related to the introduction of a magnetic phase, which differently interacts with aqueous buffered solutions. mMZN-8-BPODE shows very negative values of the surface charges; the presence of several polyanionic BPODE molecules that modify the surface of the mMZNs, thanks to the high charge, prevent aggregation and ensure high colloidal stability for several days. It is worth noticing that, in the pH range 4−9, modification with bis(phosphonic acid) provides the nanoparticles with a superficial negative charge with an overall potential below −20 mV, which is highly responsible for the good colloidal stability. Moreover, repeated measurements on the same samples showed good reproducibility of the colloidal solutions, as was clearly demonstrated by the rather small error scale bar for each ζ-potential data point.

Functionalization of the particles is also confirmed by variation of the magnetic hysteresis loops (Figure S21) recorded at 5 K due to the interaction of BPODE with cobalt ferrite on the surface of the nanoparticles, as was already reported in the literature,[71−73] as well as EDX measurements

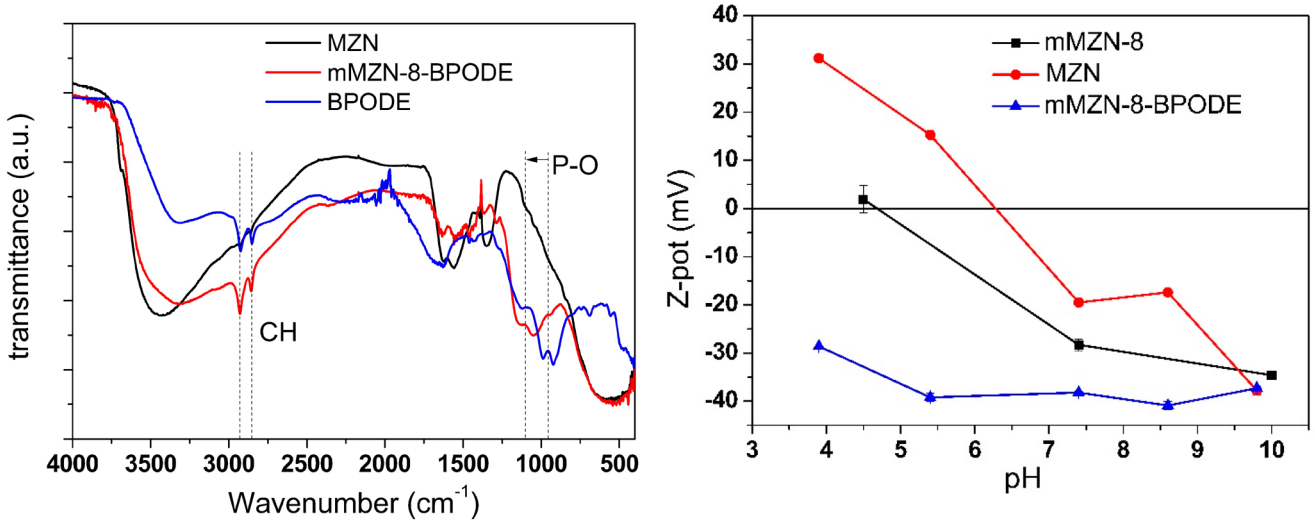

Figure 4. Left: DRIFT- IR spectra (a) of MZN (black line), BPODE (blue line), and MZN-BPODE (red line). Right: ζ-potential (b) titrations of MZN (red line), mMZN-8 (black line), and mMZN-BPODE (blue line).

https://dx.doi.org/10.1021/acsanm.9b01982
ACS Appl. Nano Mater. 2020, 3, 1232−1241

(Figure S22) that show the sulfur peak at 2.30 keV in the mMZN-BPODE spectrum, a peak that is evident when compared with the pattern of the unmodified MZN.

For plasmonic applications, mMZN-8 functionalized with BPODE was coupled with AuNPs obtained by laser ablation (see the Experimental Section). The TEM and FE-SEM images, reported in Figure 5, clearly show the presence of the AuNPs on the surface of the mMZN-8 nanoparticles.

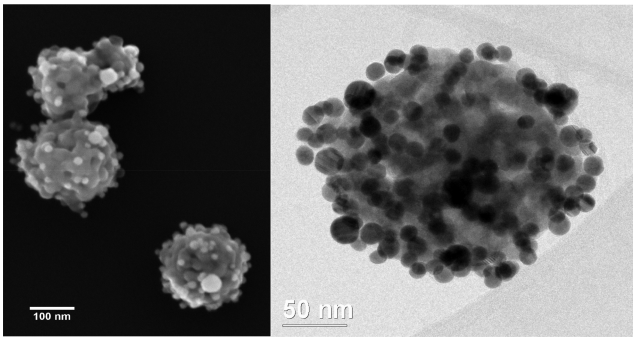

Figure 5. FE-SEM (left) and TEM (right) images of mMZN-8@AuNPs.

An important property of magnetoplasmonic nanoparticles is their mobility in a magnetic gradient, which can be exploited for applications in different research fields like increasing signals of the analytes or for cell separation.[7]

Particle migration, under a magnetic gradient, can be followed with UV−vis extinction variation of the corresponding colloidal solution.[21] Then, changes of the recorded extinction spectrum can be fitted considering the attraction force generated by the magnetic gradient and the viscosity of the solvent, which counterbalance the accelerated motion of the particles toward the magnet.[74] The fitting of the extinction decrease, when the nanoparticles are attracted by the magnet, can be obtained considering the distribution of the nanoparticle diameters recorded with SEM images.

The magnetophoretic experiment was performed by recording the extinction at λ = 370 nm, where the magnetic nanoparticles show a good extinction spectrum (Figure S23).

First, we evaluated the magnetophoretic properties of mMZN-8 Figure 6 (red points) as a function of time.

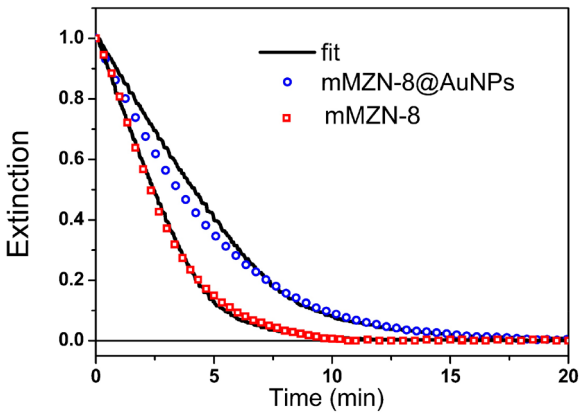

Figure 6. Magnetophoretic curves (normalized at 0 min) and their fittings for mMZN-8 (red) and mMZN@AuNPs (blue) with the parameter values reported in Table S2.

The fitting was obtained with the parameters reported in Table S2. A parameter of the fitting is the percentage of the magnetic phase, observing that the fitting suggests a value very similar to that obtained with the XRD measurements (Table 2). The nanoparticles show a good response to the magnetic gradient because, in only 6 min, more than 90% was recovered within 3 mm from the magnet and almost 100% after 10 min.

The same experiment was performed with the mMZN@AuNP magnetoplasmonic nanostructures. The extinction spectra of MZN@AuNPs and of mMZN-8@AuNPs show the characteristic bands of aggregated AuNPs, namely, a plasmonic band around 520−550 nm, also observed for isolated AuNP, and other plasmonic bands at longer wavelengths (600−800 nm), characteristic of aggregated AuNPs[31] (Figure S24). Aggregation of the nanoparticles is very important because hot spots, where SERS is particularly enhanced, are created between the nanoparticles (see below).

The extinction data at 370 nm for the magnetophoretic experiment with mMZN@AuNPs and their fittings (see the parameter values in Table S2) are reported in Figure 6 (blue points). It is possible to observe that the hydrodynamic diameter obtained is larger than that in the previous case, which is justified by the different hydrodynamic diameters of the particles with AuNPs on their surface. The magnetophoretic response of mMZN@AuNPs is always good because almost 100% of the particles was recovered within 18 min.

mMZN@AuNPs were then functionalized with thiolated malachite green (MG-SH): Figure 7a shows the SERS spectrum of the obtained nanostructures, with the characteristic band of MG-SH at 1617 cm^{-1}.[32]

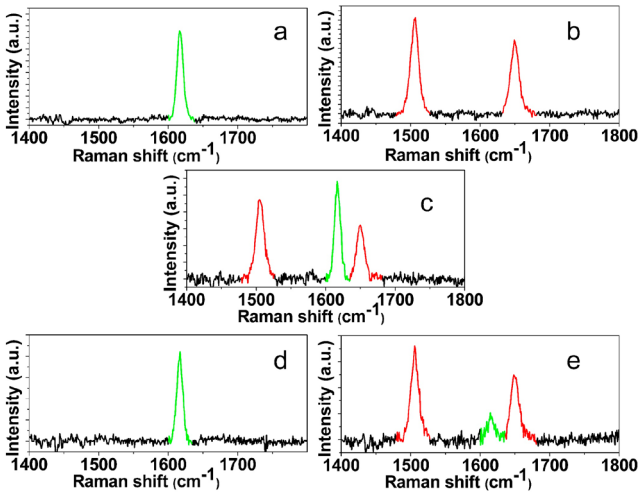

Figure 7. Raman spectra of (a) mMZN@AuNP-MG, (b) MZN@AuNP-TR, and (c) MZN@AuNP-TR and mMZN@AuNP-MG mixed together. (d and e) Raman spectra after magnetic sorting of the two systems mMZN@AuNP-MG and MZN@AuNP-TR, respectively.

The nonmagnetic MZNs were also functionalized with AuNPs, providing MZN@AuNPs (see the Experimental Section) after functionalization with BPODE. The extinction spectrum of these nanoparticles, as in the case of mMZN@AuNPs, shows that aggregated AuNPs were present (Figure S24). MZN@AuNPs were functionalized with a different SERS reporter, thiolated Texas Red (TR-SH), and in Figure 7b is reported the SERS spectrum of these nanoparticles, with the characteristic bands of TR-SH[3,7] at 1504 and 1650 cm^{-1}.

https://dx.doi.org/10.1021/acsanm.9b01982
ACS Appl. Nano Mater. 2020, 3, 1232−1241

The strong SERS spectra of mMZN@AuNPs and of MZN@AuNPs show that these nanocomposites can be used as efficient SERS tags for applications in which their presence has to be monitored like in tumor cell targeting.[7,32]

The extinction spectrum of the ZrO_2 nanoparticles with AuNPs aggregated onto their surface and SERS enhancement in the hot spots of these aggregates can be calculated with a boundary element method (BEM) calculation.[31,75,76] A model structure for the calculation considers a ZrO_2 sphere with a diameter of 200 nm and seven AuNPs of 25 nm each, organized like a "flower" on the surface of the zirconia sphere, at a distance of 0.5 nm from each other (Figure S25). This distance is appropriate for AuNPs, which are nearly in contact to avoid quantistic coupling effects.[31] The calculated spectra (absorption, scattering, and their sum, extinction) for this structure are reported in Figure S26a. These spectra show that the scattering component due to the ZrO_2 particles is the most important contribution to the extinction spectrum and that the small absorbance component is mostly due to the AuNP "flower". This is evident from the calculated spectra reported in Figure S26b for an isolated "flower".

The same BEM calculations allow evaluation of the enhancement of the SERS spectrum. The largest enhancement is found, as expected, within the gaps between the AuNPs (the so-called hot spots). With an excitation line at 633 nm, one calculates, for the AuNP "flower" on the ZrO_2 sphere, a SERS enhancement value of 4.0×10^{10}. The calculated enhancement is characteristic of the cluster of AuNPs and shows that the presence of the ZrO_2 sphere has a small influence on the SERS enhancement because for the isolated flower one calculates an enhancement of 5.8×10^{10}.

A proof-of-concept experiment for exploiting the magnetic properties of mMZN@AuNPs was conducted by mixing these nanostructures with MZN@AuNPs and then operating a magnetic sorting. The efficiency of the separation can thus be monitored with the signals of the SERS reporters of the two nanostructures.

Magnetic separation was performed with four magnets (Supermagnete S-5-25-N; D = 5 mm diameter and h = 25 mm height) on the side of a small vial containing the colloidal solution for 1 h.

Then, the solution was separated from the nanostructures attracted by the magnets. The SERS spectrum of the solution is reported in Figure 7c, whereas the spectrum of the nanostructures attracted by the magnets and dispersed again in water is reported in Figure 7d.

It is clear that the spectrum of the nanostructures present in solution (Figure 7e) shows the SERS signals of TR-SH at 1504 and 1650 cm^{-1} and only a small signal of MG-SH at 1617 cm^{-1}, whereas the nanostructures attracted by the magnets (Figure 7d) show only the spectrum of MG-SH at 1617 cm^{-1}. The separation is very satisfactory considering that the residual signal of MG-SH in the solution of nonattracted nanoparticles derives from the difficulty of pipetting the solution without perturbing the nanoparticles attracted by the magnet.

Separation of the nanostructures can be considered to be quite satisfactory also referring to the high efficiency of the SERS spectra, which allows the detection of a very small quantity of SERS reporters.

CONCLUSION

This work reports a new strategy based on MZNs for the construction of a new nanotool exploiting both the magnetic and plasmonic properties. This was obtained through the synthesis and characterization of cobalt ferrites/zirconia nanocomposites, showing magnetic properties comparable to those of bulk cobalt−iron oxides. A deep investigation was performed for a better understanding of their physical−chemical properties, such as crystal structures and magnetic properties. The spherical nanoparticles were modified with a thiol-functionalized bis(phosphonic acid), which was used to link AuNPs, obtaining nanostructures with magnetic and plasmonic properties. It is worth noticing that the use of thiol-containing bis(phosphonic acid) as a grafting unit to join together the zirconia and AuNPs is a new straightforward approach simply based on the addition of an organic linker in solution endowed with specific organic functional groups, while more traditional methods are based on chemical functionalization via organosilane derivatives, requiring longer multistep functionalization procedures. The nanostructures were further functionalized with SERS reporters. Magnetophoresis characterizations were performed, highlighting the possibility of a fast recovery, using a commercial magnet, of all of the nanostructures. BEM calculations showed, and experimental spectra confirmed, that the magnetoplasmonic nanostructures provide strong SERS signals like those for the isolated plasmonic nanostructures. Experiments for the separation of magnetic and nonmagnetic systems were very satisfactory, opening the possibility of using these nanostructures for the controlled separation of specific biological moieties in complex matrixes like CTCs in whole blood. Such applications, as well as the use of the nanostructures for therapeutic applications like drug delivery or photo/magnetothermal therapies, which will make these nanostructures theranostic agents, will be further investigated.

ASSOCIATED CONTENT

Supporting Information

The Supporting Information is available free of charge at https://pubs.acs.org/doi/10.1021/acsanm.9b01982.

Detailed synthesis of bis(phosphonic acid) and NMR characterizations, TEM and SEM images of the synthesized nanoparticles, PXRD pattern of mMZN-8 compared to those related to t-ZrO_2 (ICSD 164862), m-ZrO_2 (ICSD 417639), and $CoFe_2O_4$ (ICSD 41257), hysteresis loops at 5 K of mMZN-8 and the functionalized mMZN-8-BPODE, EDX spectra of the functionalized MZN-BPODE, N_2 physisorption of MZN and mMZN-8, extinction spectra of MZN and mMZN-8, and models for the calculation of extinction spectra (PDF)

AUTHOR INFORMATION

Corresponding Author

Pietro Riello − *Department of Molecular Sciences and Nanosystems, Università Ca' Foscari Venezia, 30170 Mestre, Venezia, Italy;* orcid.org/0000-0002-6087-3802; Email: riellop@unive.it

Authors

Anna Del Tedesco − *Department of Molecular Sciences and Nanosystems, Università Ca' Foscari Venezia, 30170 Mestre, Venezia, Italy; Department of Translational Research, National Cancer Institute−CRO-IRCSS, 33081 Aviano, Italy;* orcid.org/0000-0002-3433-6472

https://dx.doi.org/10.1021/acsanm.9b01982
ACS Appl. Nano Mater. 2020, 3, 1232−1241

Valentina Piotto − *Nanostructures and Optics Laboratory, Department of Chemical Sciences, University of Padova, 35131 Padova, Italy*
Gabriele Sponchia − *Department of Molecular Sciences and Nanosystems, Università Ca' Foscari Venezia, 30170 Mestre, Venezia, Italy*
Khohinur Hossain − *Department of Molecular Sciences and Nanosystems, Università Ca' Foscari Venezia, 30170 Mestre, Venezia, Italy*
Lucio Litti − *Nanostructures and Optics Laboratory, Department of Chemical Sciences, University of Padova, 35131 Padova, Italy;* orcid.org/0000-0001-6247-5456
Davide Peddis − *Institute of Structure of Matter, National Research Council, 00015 Monterotondo Scalo, Rome, Italy; Department of Chemistry and Industrial Chemistry, Università of Genova, 16146 Genova, Italy;* orcid.org/0000-0003-0810-8860
Alessandro Scarso − *Department of Molecular Sciences and Nanosystems, Università Ca' Foscari Venezia, 30170 Mestre, Venezia, Italy;* orcid.org/0000-0001-6114-9181
Moreno Meneghetti − *Nanostructures and Optics Laboratory, Department of Chemical Sciences, University of Padova, 35131 Padova, Italy;* orcid.org/0000-0003-3355-4811
Alvise Benedetti − *Department of Molecular Sciences and Nanosystems, Università Ca' Foscari Venezia, 30170 Mestre, Venezia, Italy*

Complete contact information is available at: https://pubs.acs.org/10.1021/acsanm.9b01982

Author Contributions

The manuscript was written through contributions of all authors. All authors have given approval to the final version of the manuscript.

Notes

The authors declare no competing financial interest.

■ ACKNOWLEDGMENTS

This work was supported by Project P-DiSC 04BIRD2016-UNIPD of the University of Padova.

■ REFERENCES

(1) Biscaglia, F.; Ripani, G.; Rajendran, S.; Benna, C.; Mocellin, S.; Bocchinfuso, G.; Meneghetti, M.; Palleschi, A.; Gobbo, M. Gold Nanoparticle Aggregates Functionalized with Cyclic RGD Peptides for Targeting and Imaging of Colorectal Cancer Cells. *ACS Applied Nano Materials* **2019**, *2*, 6436−6444.
(2) Amendola, V.; Scaramuzza, S.; Agnoli, S.; Granozzi, G.; Meneghetti, M.; Campo, G.; Bonanni, V.; Pineider, F.; Sangregorio, C.; Ghigna, P.; Polizzi, S.; Riello, P.; Fiameni, S.; Nodari, L. Laser Generation of Iron-Doped Silver Nanotruffles With Magnetic and Plasmonic Properties. *Nano Res.* **2015**, *8*, 4007−4023.
(3) Biscaglia, F.; Rajendran, S.; Conflitti, P.; Benna, C.; Sommaggio, R.; Litti, L.; Mocellin, S.; Bocchinfuso, G.; Rosato, A.; Palleschi, A.; Nitti, D.; Gobbo, M.; Meneghetti, M. Enhanced EGFR Targeting Activity of Plasmonic Nanostructures with Engineered GE11 Peptide. *Adv. Healthcare Mater.* **2017**, *6*, 1700596.
(4) Bao, Y.; Wen, T.; Samia, A. C. S.; Khandhar, A.; Krishnan, K. M. Magnetic Nanoparticles: Material Engineering and Emerging Applications in Lithography and Biomedicine. *J. Mater. Sci.* **2016**, *51*, 513−553.
(5) Shi, X.; Xiang, C.; Liu, Y.; Lin, H.; Xu, Y.; Ji, J. Preparation And Evaluation of Chitosan/B-Cyclodextrin Magnetic Nanoparticles as a Photodegradable And Hydrophobic Drug Delivery Carrier. *J. Appl. Polym. Sci.* **2017**, *134*, 45076.
(6) Litti, L.; Ramundo, A.; Biscaglia, F.; Toffoli, G.; Gobbo, M.; Meneghetti, M. A Surface Enhanced Raman Scattering Based Colloid Nanosensor for Developing Therapeutic Drug Monitoring. *J. Colloid Interface Sci.* **2019**, *533*, 621−626.
(7) Bertorelle, F.; Pinto, M.; Zappon, R.; Pilot, R.; Litti, L.; Fiameni, S.; Conti, G.; Gobbo, M.; Toffoli, G.; Colombatti, M.; Fracasso, G.; Meneghetti, M. Safe Core-Satellite Magneto-Plasmonic Nanostructures for Efficient Targeting And Photothermal Treatment of Tumor Cells. *Nanoscale* **2018**, *10*, 976−984.
(8) Wang, L.; Park, H.-Y.; Lim, S. I. I.; Schadt, M. J.; Mott, D.; Luo, J.; Wang, X.; Zhong, C.-J. Core@Shell Nanomaterials: Gold-Coated Magnetic Oxide Nanoparticles. *J. Mater. Chem.* **2008**, *18*, 2629−2635.
(9) Huang, J.; Li, Y.; Orza, A.; Lu, Q.; Guo, P.; Wang, L.; Yang, L.; Mao, H. Magnetic Nanoparticle Facilitated Drug Delivery for Cancer Therapy with Targeted and Image-Guided Approaches. *Adv. Funct. Mater.* **2016**, *26*, 3818−3836.
(10) Zamani, M.; Hocini, A. Potential Of Sio2/Zro2 Matrix Doped with CoFe2O4 Magnetic Nanoparticles in Achieving Integrated Magneto-Optical Isolators. *Photonics and Nanostructures - Fundamentals and Applications* **2017**, *24*, 41−46.
(11) Liu, W.; Wang, D.; Duan, Y.; Zhang, Y.; Bian, F. Palladium Supported On Poly (Ionic Liquid) Entrapped Magnetic Nanoparticles as a Highly Efficient and Reusable Catalyst for The Solvent-Free Heck Reaction. *Tetrahedron Lett.* **2015**, *56*, 1784−1789.
(12) Sarina, S.; Zhu, H.; Jaatinen, E.; Xiao, Q.; Liu, H.; Jia, J.; Chen, C.; Zhao, J. Enhancing Catalytic Performance of Palladium in Gold and Palladium Alloy Nanoparticles for Organic Synthesis Reactions through Visible Light Irradiation at Ambient Temperatures. *J. Am. Chem. Soc.* **2013**, *135*, 5793−5801.
(13) Alex, D.; Mathew, A.; Sukumaran, R. K. Esterases Immobilized on Aminosilane Modified Magnetic Nanoparticles as a Catalyst for Biotransformation Reactions. *Bioresour. Technol.* **2014**, *167*, 547−550.
(14) Silvestri, A.; Mondini, S.; Marelli, M.; Pifferi, V.; Falciola, L.; Ponti, A.; Ferretti, A. M.; Polito, L. Synthesis of Water Dispersible and Catalytically Active Gold-Decorated Cobalt Ferrite Nanoparticles. *Langmuir* **2016**, *32*, 7117−7126.
(15) Rashid, Z.; Soleimani, M.; Ghahremanzadeh, R.; Vossoughi, M.; Esmaeili, E. Effective Surface Modification of MnFe2O4@SiO2@PMIDA Magnetic Nanoparticles for Rapid and High-Density Antibody Immobilization. *Appl. Surf. Sci.* **2017**, *426*, 1023−1029.
(16) Chandra, S.; Patel, M. D.; Lang, H.; Bahadur, D. Dendrimer-Functionalized Magnetic Nanoparticles: a New Electrode Material for Electrochemical Energy Storage Devices. *J. Power Sources* **2015**, *280*, 217−226.
(17) Kadasala, N. R.; Wei, A. Trace Detection of Tetrabromobisphenol A by SERS with DMAP-Modified Magnetic Gold Nanoclusters. *Nanoscale* **2015**, *7* (25), 10931−10935.
(18) La Porta, A.; Sanchez-Iglesias, A.; Altantzis, T.; Bals, S.; Grzelczak, M.; Liz-Marzan, L. M. Multifunctional Self-Assembled Composite Colloids and Their Application to SERS Detection. *Nanoscale* **2015**, *7* (23), 10377−10381.
(19) Maccaferri, N.; Gregorczyk, K. E.; de Oliveira, T.; Kataja, M.; van Dijken, S.; Pirzadeh, Z.; Dmitriev, A.; Akerman, J.; Knez, M.; Vavassori, P. Ultrasensitive and Label-Free Molecular-Level Detection Enabled by Light Phase Control in Magnetoplasmonic Nanoantennas. *Nat. Commun.* **2015**, *6*, 6150.
(20) Sepulveda, B.; Calle, A.; Lechuga, L. M.; Armelles, G. Highly Sensitive Detection of Biomolecules with the Magneto-Optic Surface-Plasmon-Resonance Sensor. *Opt. Lett.* **2006**, *31*, 1085−1087.
(21) Leung, K. C.-F.; Xuan, S.; Zhu, X.; Wang, D.; Chak, C.-P.; Lee, S.-F.; Ho, W. K. W.; Chung, B. C. T. Gold and Iron Oxide Hybrid Nanocomposite Materials. *Chem. Soc. Rev.* **2012**, *41*, 1911−1928.
(22) Sabale, S.; Kandesar, P.; Jadhav, V.; Komorek, R.; Motkuri, R. K.; Yu, X.-Y. Recent Developments in The Synthesis, Properties, and Biomedical Applications of Core/Shell Superparamagnetic Iron Oxide Nanoparticles With Gold. *Biomater. Sci.* **2017**, *5*, 2212−2225.
(23) Ravichandran, M.; Oza, G.; Velumani, S.; Ramirez, J. T.; Garcia-Sierra, F.; Andrade, N. B.; Vera, A.; Leija, L.; Garza-Navarro,

M. A. Plasmonic/Magnetic Multifunctional Nanoplatform for Cancer Theranostics. *Sci. Rep.* **2016**, *6*, 34874.
(24) Jagminas, A.; Mažeika, K.; Kondrotas, R.; Kurtinaitienė, M.; Jagminienė, A.; Mikalauskaitė, A. Functionalization of Cobalt Ferrite Nanoparticles by a Vitamin C-Assisted Covering with Gold. *Nanomater. Nanotechnol.* **2014**, *4*, 11.
(25) Karimi, Z.; Karimi, L.; Shokrollahi, H. Nano-Magnetic Particles Used in Biomedicine: Core and Coating Materials. *Mater. Sci. Eng., C* **2013**, *33*, 2465−2475.
(26) Fan, Z.; Shelton, M.; Singh, A. K.; Senapati, D.; Khan, S. A.; Ray, P. C. Multifunctional Plasmonic Shell-Magnetic Core Nanoparticles for Targeted Diagnostics, Isolation, and Photothermal Destruction of Tumor Cells. *ACS Nano* **2012**, *6*, 1065−1073.
(27) Bertorelle, F.; Ceccarello, M.; Pinto, M.; Fracasso, G.; Badocco, D.; Amendola, V.; Pastore, P.; Colombatti, M.; Meneghetti, M. Efficient AuFeOx Nanoclusters of Laser-Ablated Nanoparticles in Water for Cells Guiding and Surface-Enhanced Resonance Raman Scattering Imaging. *J. Phys. Chem. C* **2014**, *118*, 14534−14541.
(28) Litti, L.; Rivato, N.; Fracasso, G.; Bontempi, P.; Nicolato, E.; Marzola, P.; Venzo, A.; Colombatti, M.; Gobbo, M.; Meneghetti, M. A SERRS/MRI Multimodal Contrast Agent Based on Naked Au Nanoparticles Functionalized with a Gd(Iii) Loaded PEG Polymer for Tumor Imaging and Localized Hyperthermia. *Nanoscale* **2018**, *10*, 1272−1278.
(29) Biscaglia, F.; Quarta, S.; Villano, G.; Turato, C.; Biasiolo, A.; Litti, L.; Ruzzene, M.; Meneghetti, M.; Pontisso, P.; Gobbo, M. Pres1 Peptide-Functionalized Gold Nanostructures with SERRS Tags for Efficient Liver Cancer Cell Targeting. *Mater. Sci. Eng., C* **2019**, *103*, 109762.
(30) Nie, S.; Emory, S. R. Probing Single Molecules and Single Nanoparticles by Surface-Enhanced Raman Scattering. *Science* **1997**, *275*, 1102−1106.
(31) Litti, L.; Meneghetti, M. Predictions on the SERS Enhancement Factor of Gold Nanosphere Aggregate Samples. *Phys. Chem. Chem. Phys.* **2019**, *21*, 15515−15522.
(32) Meneghetti, M.; Scarsi, A.; Litti, L.; Marcolongo, G.; Amendola, V.; Gobbo, M.; Di Chio, M.; Boscaini, A.; Fracasso, G.; Colombatti, M. Plasmonic Nanostructures for SERRS Multiplexed Identification of Tumor-Associated Antigens. *Small* **2012**, *8*, 3733−3738.
(33) Bechta, S. V.; Krushinov, E. V.; Almjashev, V. I.; Vitol, S. A.; Mezentseva, L. P.; Petrov, Y. B.; Lopukh, D. B.; Khabensky, V. B.; Barrachin, M.; Hellmann, S.; Froment, K.; Fischer, M.; Tromm, W.; Bottomley, D.; Defoort, F.; Gusarov, V. V. Phase Diagram of The Zro2-FeO System. *J. Nucl. Mater.* **2006**, *348*, 114−121.
(34) Kuryliszyn-Kudelska, I.; Arciszewska, M.; Małolepszy, A.; Mazurkiewicz, M.; Stobinski, L.; Grabias, A.; Kopcewicz, M.; Paszkowicz, W.; Minikaev, R.; Domukhovski, V.; Nedelko, N.; Dobrowolski, W. Influence of Fe Doping on Magnetic Properties of Zro2 Nanocrystals. *J. Alloys Compd.* **2015**, *632*, 609−616.
(35) Navío; Hidalgo; Colón, G.; Botta, S. G.; Litter, M. I. Preparation and Physicochemical Properties of ZrO2 and Fe/ZrO2 Prepared by a Sol-Gel Technique. *Langmuir* **2001**, *17*, 202−210.
(36) Kumar, S.; Bhunia, S.; Singh, J.; Ojha, A. K. Absence of Room Temperature Ferromagnetism in Fe Stabilized Zro2 Nanostructures and Effect of Fe Doping on Its Structural, Optical and Luminescence Properties. *J. Alloys Compd.* **2015**, *649*, 348−356.
(37) Chattopadhyay, S.; Dash, S. K.; Tripathy, S.; Das, B.; Mandal, D.; Pramanik, P.; Roy, S. Toxicity of Cobalt Oxide Nanoparticles to Normal Cells; An In Vitro And In Vivo Study. *Chem.-Biol. Interact.* **2015**, *226*, 58−71.
(38) Leyssens, L.; Vinck, B.; Van Der Straeten, C.; Wuyts, F.; Maes, L. Cobalt Toxicity in Humans—A Review of the Potential Sources and Systemic Health Effects. *Toxicology* **2017**, *387*, 43−56.
(39) Simonsen, L. O.; Harbak, H.; Bennekou, P. Cobalt Metabolism and Toxicology—A Brief Update. *Sci. Total Environ.* **2012**, *432*, 210−215.
(40) Peddis, D.; Cannas, C.; Musinu, A.; Ardu, A.; Orru, F.; Fiorani, D.; Laureti, S.; Rinaldi, D.; Muscas, G.; Concas, G.; Piccaluga, G. Beyond The Effect of Particle Size: Influence of Cofe2o4 Nanoparticle Arrangements on Magnetic Properties. *Chem. Mater.* **2013**, *25*, 2005−2013.
(41) Peddis, D.; Cannas, C.; Musinu, A.; Piccaluga, G. Magnetism in Nanoparticles: Beyond the Effect of Particle Size. *Chem. - Eur. J.* **2009**, *15*, 7822−7829.
(42) Muscas, G.; Singh, G.; Glomm, W. R.; Mathieu, R.; Kumar, P. A.; Concas, G.; Agostinelli, E.; Peddis, D. Tuning The Size And Shape Of Oxide Nanoparticles by Controlling Oxygen Content in the Reaction Environment: Morphological Analysis by Aspect Maps. *Chem. Mater.* **2015**, *27*, 1982−1990.
(43) Parma, A.; Freris, I.; Riello, P.; Cristofori, D.; de Julian Fernandez, C.; Amendola, V.; Meneghetti, M.; Benedetti, A. Structural and Magnetic Properties of Mesoporous SiO2 Nanoparticles Impregnated with Iron Oxide or Cobalt-Iron Oxide Nanocrystals. *J. Mater. Chem.* **2012**, *22*, 19276−19288.
(44) Amendola, V.; Meneghetti, M. Controlled Size Manipulation of Free Gold Nanoparticles by Laser Irradiation and Their Facile Bioconjugation. *J. Mater. Chem.* **2007**, *17*, 4705−4710.
(45) Kim, J.; Park, S.; Lee, J. E.; Jin, S. M.; Lee, J. H.; Lee, I. S.; Yang, I.; Kim, J.-S.; Kim, S. K.; Cho, M.-H.; Hyeon, T. Designed Fabrication of Multifunctional Magnetic Gold Nanoshells and Their Application to Magnetic Resonance Imaging and Photothermal Therapy. *Angew. Chem.* **2006**, *118*, 7918−7922.
(46) Perrin, D. D.; Armarego, W. L. F. *Purification of laboratory chemicals*, 3th ed.; Pergamon Press, 1993.
(47) Still, W. C.; Kahn, M.; Mitra, A. Rapid Chromatographic Technique for Preparative Separations with Moderate Resolution. *J. Org. Chem.* **1978**, *43*, 2923−2925.
(48) Sponchia, G.; Ambrosi, E.; Rizzolio, F.; Hadla, M.; Del Tedesco, A.; Russo Spena, C.; Toffoli, G.; Riello, P.; Benedetti, A. Biocompatible Tailored Zirconia Mesoporous Nanoparticles with High Surface Area for Theranostic Applications. *J. Mater. Chem. B* **2015**, *3*, 7300−7306.
(49) Granchi, D.; Scarso, A.; Bianchini, G.; Chiminazzo, A.; Minto, A.; Sgarbossa, P.; Michelin, R. A.; Di Pompo, G.; Avnet, S.; Strukul, G. Low Toxicity and Unprecedented Anti-Osteoclast Activity of a Simple Sulfur-Containing Gem-Bisphosphonate: a Comparative Study. *Eur. J. Med. Chem.* **2013**, *65*, 448−455.
(50) Schindelin, J.; Arganda-Carreras, I.; Frise, E.; Kaynig, V.; Longair, M.; Pietzsch, T.; Preibisch, S.; Rueden, C.; Saalfeld, S.; Schmid, B.; Tinevez, J.-Y.; White, D. J.; Hartenstein, V.; Eliceiri, K.; Tomancak, P.; Cardona, A. Fiji: An Open-Source Platform for Biological-Image Analysis. *Nat. Methods* **2012**, *9*, 676−682.
(51) Schneider, C. A.; Rasband, W. S.; Eliceiri, K. W. NIH Image To Imagej: 25 Years Of Image Analysis. *Nat. Methods* **2012**, *9* (7), 671−675.
(52) Enzo, S.; Polizzi, S.; Benedetti, A. Applications of Fitting Techniques to the Warren-Averbach Method for X-Ray Line Broadening Analysis. *Zeitschrift für Kristallographie-Crystalline Materials* **1985**, *170*, 275−288.
(53) Brunauer, S.; Emmett, P. H.; Teller, E. Adsorption of Gases in Multimolecular Layers. *J. Am. Chem. Soc.* **1938**, *60*, 309−319.
(54) Barrett, E. P.; Joyner, L. G.; Halenda, P. P. The Determination of Pore Volume And Area Distributions in Porous Substances. I. Computations From Nitrogen Isotherms. *J. Am. Chem. Soc.* **1951**, *73*, 373−380.
(55) Sing, K.; Everett, D.; Haul, R.; Moscou, L.; Pierotti, R.; Rouquerol, J.; Siemieniewska, T. Commission on Colloid and Surface Chemistry Including Catalysis. *Pure Appl. Chem.* **1985**, *57*, 603−619.
(56) Freris, I.; Riello, P.; Enrichi, F.; Cristofori, D.; Benedetti, A. Synthesis and Optical Properties of Sub-Micron Sized Rare Earth-Doped Zirconia Particles. *Opt. Mater.* **2011**, *33*, 1745−1752.
(57) Parma, A.; Freris, I.; Riello, P.; Enrichi, F.; Cristofori, D.; Benedetti, A. Structural and Photoluminescence Properties of ZrO2:Eu3+ @ SiO2 Nanophosphors as a Function of Annealing Temperature. *J. Lumin.* **2010**, *130*, 2429−2436.

https://dx.doi.org/10.1021/acsanm.9b01982
ACS Appl. Nano Mater. 2020, 3, 1232−1241

(58) Choudhary, V. R.; Banerjee, S.; Pataskar, S. G. Combustion Of Dilute Propane Over Transition Metal-Doped ZrO2 (Cubic) Catalysts. *Appl. Catal., A* **2003**, *253*, 65−74.
(59) Anku, W. W.; Oppong, S. O.-B.; Shukla, S. K.; Agorku, E. S.; Govender, P. P. Cobalt Doped Zro2 Decorated Multiwalled Carbon Nanotube: A Promising Nanocatalyst for Photodegradation of Indigo Carmine and Eosin Y Dyes. *Prog. Nat. Sci.* **2016**, *26*, 354−361.
(60) Sangalli, D.; Cianci, E.; Lamperti, A.; Ciprian, R.; Albertini, F.; Casoli, F.; Lupo, P.; Nasi, L.; Campanini, M.; Debernardi, A. Exploiting Magnetic Properties of Fe Doping in Zirconia. *Eur. Phys. J. B* **2013**, *86*, 1−6.
(61) Cannas, C.; Musinu, A.; Peddis, D.; Piccaluga, G. New Synthesis of Ferrite-Silica Nanocomposites by a Sol-Gel Auto-Combustion. *J. Nanopart. Res.* **2004**, *6*, 223−232.
(62) Cannas, C.; Musinu, A.; Ardu, A.; Orrù, F.; Peddis, D.; Casu, M.; Sanna, R.; Angius, F.; Diaz, G.; Piccaluga, G. CoFe2O4 and CoFe2O4/SiO2 Core/Shell Nanoparticles: Magnetic and Spectroscopic Study. *Chem. Mater.* **2010**, *22*, 3353−3361.
(63) Grigorova, M.; Blythe, H. J.; Blaskov, V.; Rusanov, V.; Petkov, V.; Masheva, V.; Nihtianova, D.; Martinez, L. M.; Muñoz, J. S.; Mikhov, M. Magnetic Properties and Mössbauer Spectra of Nanosized CoFe2O4 powders. *J. Magn. Magn. Mater.* **1998**, *183*, 163−172.
(64) Peddis, D. Magnetic Properties of Spinel Ferrite Nanoparticles: Influence of the Magnetic Structure. *Magnetic Nanoparticle Assemblies*; Pan Stanford, 2014; pp 159−198.
(65) Peddis, D.; Cannas, C.; Musinu, A.; Ardu, A.; Orrù, F.; Fiorani, D.; Laureti, S.; Rinaldi, D.; Muscas, G.; Concas, G.; Piccaluga, G. Beyond the Effect of Particle Size: Influence of CoFe2O4 Nanoparticle Arrangements on Magnetic Properties. *Chem. Mater.* **2013**, *25*, 2005−2013.
(66) Peddis, D.; Orrù, F.; Ardu, A.; Cannas, C.; Musinu, A.; Piccaluga, G. Interparticle Interactions and Magnetic Anisotropy in Cobalt Ferrite Nanoparticles: Influence of Molecular Coating. *Chem. Mater.* **2012**, *24*, 1062−1071.
(67) Del Tedesco, A.; Ambrosi, E.; Borsacchi, S.; Benedetti, A. Functionalization of Mesoporous Silica Nanoparticles with Organosilanes: Experimental Evidence of the Interaction Between Organic Groups and Silica Surface. *Curr. Org. Chem.* **2017**, *21*, 2434−2444.
(68) Malba, C.; Sudhakaran, U. P.; Borsacchi, S.; Geppi, M.; Enrichi, F.; Natile, M. M.; Armelao, L.; Finotto, T.; Marin, R.; Riello, P.; Benedetti, A. Structural and Photophysical Properties of Rare-Earth Complexes Encapsulated Into Surface Modified Mesoporous Silica Nanoparticles. *Dalton T* **2014**, *43*, 16183−16196.
(69) Basly, B.; Popa, G.; Fleutot, S.; Pichon, B. P.; Garofalo, A.; Ghobril, C.; Billotey, C.; Berniard, A.; Bonazza, P.; Martinez, H.; Felder-Flesch, D.; Begin-Colin, S. Effect Of The Nanoparticle Synthesis Method on Dendronized Iron Oxides as MRI Contrast Agents. *Dalton T* **2013**, *42*, 2146−2157.
(70) Guerrero, G.; Mutin, P. H.; Vioux, A. Anchoring of Phosphonate and Phosphinate Coupling Molecules on Titania Particles. *Chem. Mater.* **2001**, *13*, 4367−4373.
(71) Salafranca, J.; Gazquez, J.; Pérez, N.; Labarta, A.; Pantelides, S. T.; Pennycook, S. J.; Batlle, X.; Varela, M. Surfactant Organic Molecules Restore Magnetism in Metal-Oxide Nanoparticle Surfaces. *Nano Lett.* **2012**, *12*, 2499−2503.
(72) Wu, W.; Wu, Z.; Yu, T.; Jiang, C.; Kim, W.-S. Recent Progress on Magnetic Iron Oxide Nanoparticles: Synthesis, Surface Functional Strategies and Biomedical Applications. *Sci. Technol. Adv. Mater.* **2015**, *16*, 023501.
(73) Vestal, C. R.; Zhang, Z. J. Synthesis and Magnetic Characterization of Mn and Co Spinel Ferrite-Silica Nanoparticles with Tunable Magnetic Core. *Nano Lett.* **2003**, *3*, 1739−1743.
(74) Yeap, S. P.; Toh, P. Y.; Ahmad, A. L.; Low, S. C.; Majetich, S. A.; Lim, J. Colloidal Stability and Magnetophoresis of Gold-Coated Iron Oxide Nanorods in Biological Media. *J. Phys. Chem. C* **2012**, *116*, 22561−22569.
(75) Myroshnychenko, V.; Carbó-Argibay, E.; Pastoriza-Santos, I.; Pérez-Juste, J.; Liz-Marzán, L. M.; García de Abajo, F. J. Modeling the Optical Response of Highly Faceted Metal Nanoparticles with a Fully 3D Boundary Element Method. *Adv. Mater.* **2008**, *20*, 4288−4293.
(76) Hohenester, U.; Trügler, A. MNPBEM - A Matlab Toolbox for the Simulation of Plasmonic Nanoparticles. *Comput. Phys. Commun.* **2012**, *183*, 370−381.

https://dx.doi.org/10.1021/acsanm.9b01982
ACS Appl. Nano Mater. 2020, 3, 1232−1241